Electron Energy Dependent Charging Effects of Multilayered Dielectric Materials

Gregory Wilson, JR Dennison, Amberly Evans and Justin Dekany

***Abstract*— Measurements of the charge distribution in electron-bombarded, thin-film, multilayer dielectric samples showed that charging of multilayered materials evolves with time and is highly dependent on incident energy; this is driven by electron penetration depth, electron emission and material conductivity. Based on the net surface potential's dependence on beam current, electron range, electron emission and conductivity, measurements of the surface potential, displacement current and beam energy allow the charge distribution to be inferred. To take these measurements, a thin-film disordered SiO_2 structure with a conductive middle layer was charged using 200 eV and 5 keV electron beams with regular 15 s pulses at 1 nA/cm^2 to 500 nA/cm^2. Results show that there are two basic charging scenarios which are consistent with simple charging models; these are analyzed using independent determinations of the material's electron range, yields, and conductivity. Large negative net surface potentials led to electrostatic breakdown and large visible arcs, which have been observed to lead to detrimental spacecraft charging effects.**

***Index Terms*—Spacecraft charging, electron emission electron range, conductivity, multilayer materials, dielectrics**

I. Introduction

This research investigates the formation and evolution of internal charge distributions produced in multilayer dielectrics by incident electron fluxes. The internal distribution of charge in materials is obviously at the root of our understanding of spacecraft charging. As spacecraft enter into the space environment, they are constantly subjected to varying levels of charge fluxes, electrons being the principle culprit [1]. If care is not taken in spacecraft design and material selection, deleterious effects may occur as the deposited charges generate electric fields large enough to cause electrostatic discharge which can often result in damage to materials, components and spacecraft. To mitigate these detrimental effects, understanding of the internal charge evolution within materials used in the construction and shielding of spacecraft is essential. Ground-based experiments serve a central role in this process, not only to validate the models, but also to characterize proposed spacecraft materials and the charging and discharging processes. While the study of materials undergoing electron bombardment is of broad interest, it is one of the pillars of spacecraft charging.

Measurements [2] of the internal charge distribution of materials exposed to electron fluxes allow the resulting electric fields to be predicted. However, such direct measurements are often not possible or practical. Inference of the charge distributions is often necessary through indirect measurements [3,4,5,6,7] or modeling [8]. Determination of surface potentials and currents flowing into and out of a material are more readily measured and provide useful evidence to determine internal charge distributions. As shown below, more indirect measurements of electron penetration depth, energy dependent electron yield and temperature dependant material conductivity are often employed. While the first two properties are highly energy dependent, the material conductivity has only slight dependence on energy (through the radiation induced conductivity (RIC) mechanism), but is highly temperature dependent. Because high insulating materials generally have higher yield rates and cannot quickly dissipate accumulated charge, they are of particular concern for spacecraft charging. Using these material properties, simple models have been developed which can predict net surface potentials, current, and the probability of electrostatic discharge. While the independent characterization of each of these individual material properties is important [9,10,11,12] it is the interplay between these processes that define the time evolution of the charge distribution [13].

We begin with a brief description of the instrumentation and

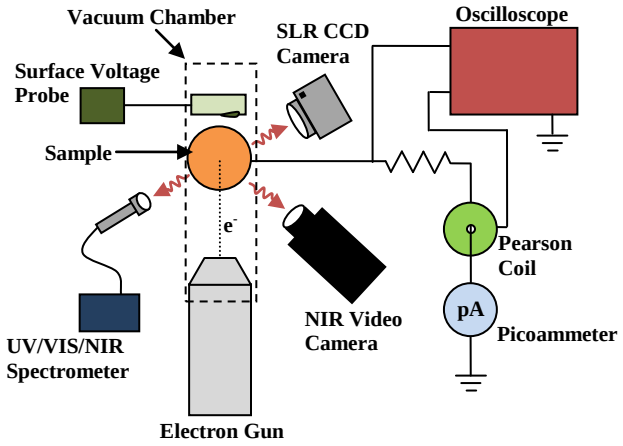

Fig. 1. Block diagram of instrumentation for collecting the pulse charging surface voltage and electrode current data induced by electron beam bombardment. Instrumentation includes picoammeters, Pearson coils, and a storage oscilloscope for electrode current measurements and UV/VIS and IR spectrometers, an SLR CCD still camera, and a NIR video camera for optical measurements.

Research was supported by funding from the NASA James Goddard Space Flight Center and a Utah State University Undergraduate Research and Creative Opportunities grant.

Greg Wilson, JR Dennison, Amberly Evans and Justin Dekany are with the Materials Physics Group in the Physics Department at Utah State University in Logan, UT 84322 USA (e-mail: GregdWilson@gmail.com, JR.Dennison@usu.edu). Evans, Wilson, and Dekany are graduate students in the Physics Department at USU. Dennison is a professor in that department.

experimental design. We present a general overview of electron range, electron yield and electron transport, and then describe their interconnectivity with the net surface potential and electrode currents. Finally, measurements for two different energy regimes which define the two resulting charging scenarios (charge deposition in the surface dielectric or conductive layer) are interpreted in terms of our multilayer model.

II. Experimentation

In order to investigate the charging of multilayer dielectric materials, pulsed charging experiments were conducted using multilayered dielectric materials of an SiO_2 based optical coating, a conductive middle layer and an SiO_2 substrate. Tests were made with the p layer both grounded and ungrounded. Experiments were conducted in the main USU electron emission ultrahigh vacuum test chamber [14], modified for observations of low intensity UV/VIS/NIR glow over a broad range of sample temperatures [15,16]. Figure 1 provides a general schematic of the experimental system used.

The samples were subjected to short pulses (t_{on}≈15 s) of electron bombardment using a monoenergetic electron beam with beam energies of either 200 eV or 5 keV. A low energy electron gun [Staib, EK-5-S1] was used, that can deliver a well-characterized, low-flux pulsed beam (typically ~50pA/cm^2 to 1 μA/cm^2) over an energy range of 20 eV to 5 keV. The defocused electron beam produced a beam profile at the sample with about ±30% uniformity over an ~3 cm diameter beam spot. Beam fluxes were monitored with a Faraday cup. Beam current densities of 20±1 nA/cm^2 at 200 eV and 2.7±1 nA/cm^2 at 5 keV were used for the experiments reported here, with an exposed sample area of 4.9±0.2 cm^2

Currents were measured from the back of the mirror to ground and between the conductive layer and ground when the conductive layer was grounded, using fast sensitive picoammeters with <0.2 pA resolution [17]. After each pulse the surface potential was measured using a high impedance non-contact electrostatic voltage probe with a range from ~1 V to ~10 kV and a resolution of ≲1.5 V; details of this instrument are given by Hodges [3,4]. The time between the pulses was limited to t_{off}≈84 s by the time required to take a surface voltage measurement. Total time for each experimental run was on the order of 1 hr or until equilibrium was reached or electrostatic breakdown was observed. To confirm that near-equilibrium was achieved, a few tests on the order of a few hours were conducted.

Samples (2.5 cm diameter) were prepared with thin film (~120 nm thick) disordered SiO_2 (fused silica) deposited on ~220 nm thick highly reflective, optically smooth metal (mostly Ag) layers on a 2.7 mm thick fused quartz substrate. The samples were optically cleaned and underwent a ~12 hr vacuum bakeout at ~390 K and <1·10^{-3} Pa while grounded to eliminate adsorbed water, volatile contaminates, and initial embedded charge. Separate samples were used for each test due to long charge dissipation times. The samples were mounted on Cu pedestals on a multi-sample carousel, and were place in an ultrahigh vacuum chamber (base pressure <1·10^{-6} Pa) for >24 hrs outgassing before measurements were made. The sample carousel was thermally anchored to (but

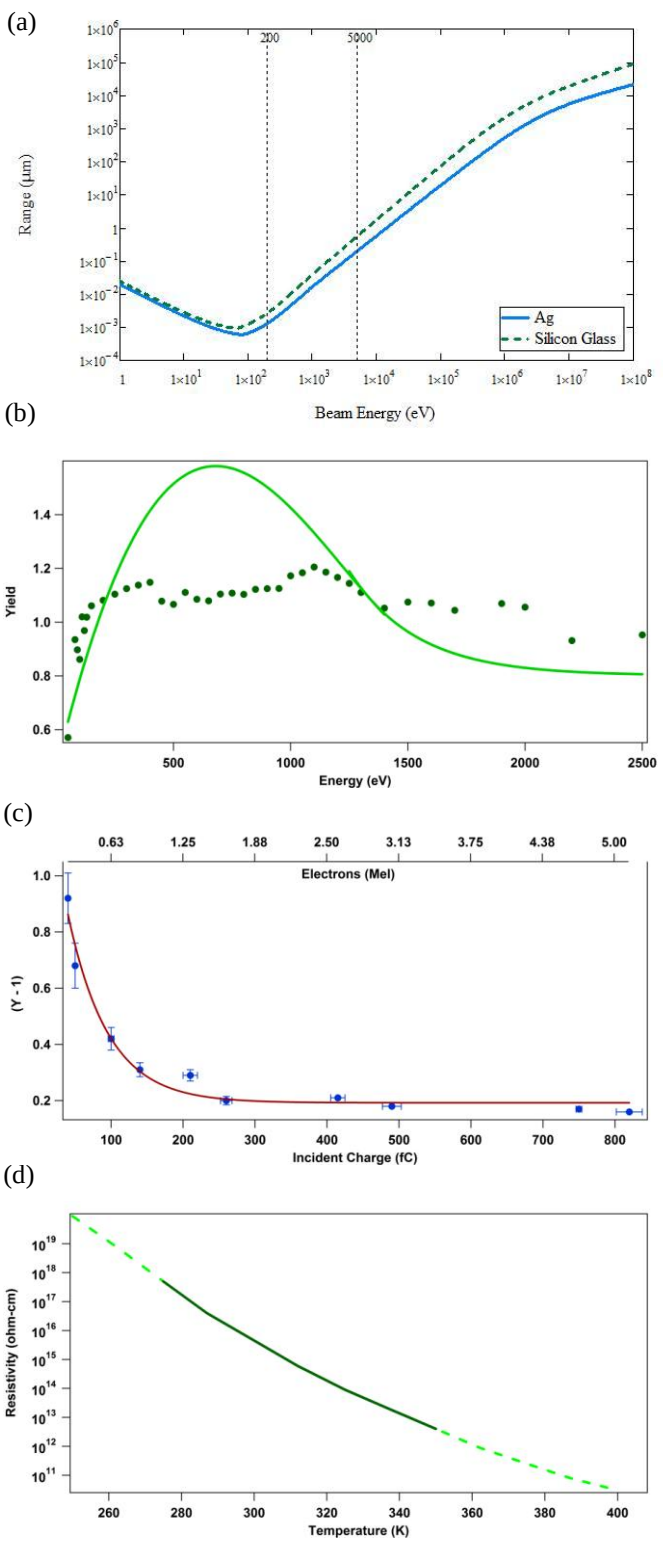

Fig. 2. Material properties of fused silica. (a) Electron range vs incident energy for disordered SiO_2 and Ag using the composite model developed by Wilson [9]. (b) Total electron yield as a function of incident energy for fused silica. Dark green points show the measured total yield, including charging effects. Green curve shows the total yield determined for negligible charging [10]. (c) Total yield of fused silica as a function of charge in the pulse used to determine the yield. Fit is an exponential decay of $[1\text{-}Y(Q;E_b)]$ for increasing incident charge, based on Eq. 1 with τ_q=56 ± 9 fC. [18,19] (d) Measured conductivity of bulk fused silica as a function of temperature.

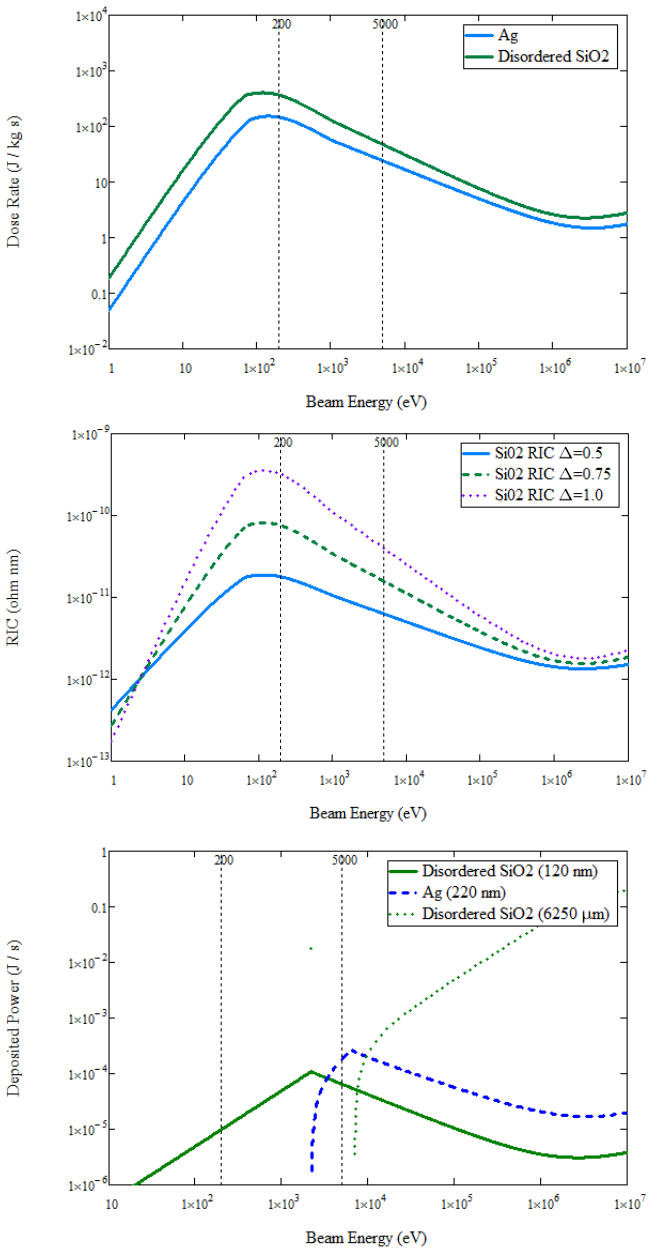

Fig. 3. (a) Estimated dose rate for Ag and disordered SiO_2 as a function of incident energy. (b) Estimated RIC as a function of incident energy. (c) Estimated deposited power for our multilayered system with a flux density of 10 nA/cm^2 and a beam area of 4.9 cm^2 as a function of incident energy. Refer to [9] for explanation of calculation methods.

electrically isolated from) a cryogen reservoir. In combination with resistive heaters and liquid N_2 cryogen, the samples were maintained over a range of temperatures from ~150 K to ~400 K with a long-term stability of ±3 K. Measurements reported in Fig. 7 were made at 298 K (and at 135 K as noted).

During these tests imaging instruments were also used to help detect arcing events, as shown in Fig. 1. Two cameras and two fiber optic spectrometers were used to monitor low light intensity and rapid flashes associated with arcs. Though not the focus of this paper, detailed studies of the optical signatures of cathodeluminescence and arcing were conducted; these results are reported elsewhere [15,16].

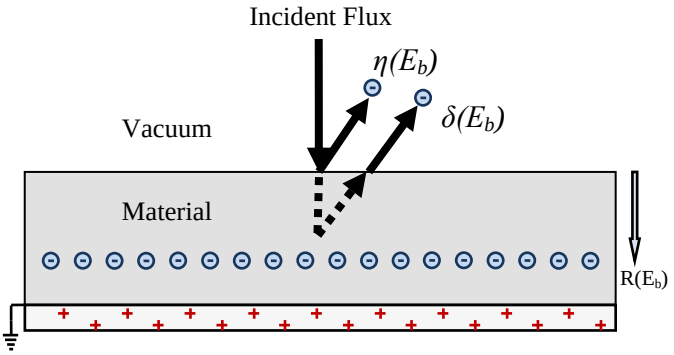

Fig. 4. Diagram of incident electron flux impinging on a generic material. $\eta(E_b)$ denotes the backscattered yield for electrons that originate within the incident beam or that have emission energies E>50 eV. $\delta(E_b)$ denotes the secondary yield for electrons liberated from within the material or that have emission energies E<50 eV. The total yield for all emission energies is the sum of the secondary and backscattered yield; $Y(E_b)= \eta(E_b)+ \delta(E_b)$. $R(E_b)$ is the incident energy-dependant electron penetration depth (range) [9].

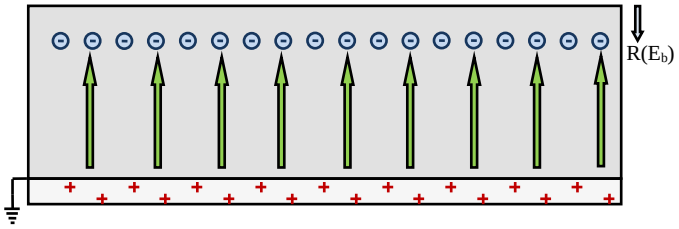

Fig. 5. Electric fields arise due to charge in the embedded layer(s) and on the grounded planes. The resulting electric field can lead to charge transport of the embedded charge layer and displacement currents resulting from charge accumulation and charge migration toward the grounded planes. How easily charge can move depends on the conductivity of the material.

III. Theoretical Model

Four experiments are considered as depicted in Fig. 6. The experiments differ in terms of the incident energy and flux, and as we will see below, produce dramatically differ results. Two experiments (a and b) use low incident energy, two consider high incident energy. Two experiments have an ungrounded conducting layer (a and c) and two have a grounded conducting layer (b and d). To interpret the experiments, we must consider three physical phenomena—the electron range, electron yield and the electron transport (conductivity) of the material—and how they are affected by the experimental conditions.

A. Electron Range

The electron range is the maximum distance an electron of a given incident energy can penetrate through a material at a given incident energy, E_b, as the incident electron undergoes a succession of energy loss collisions and ultimately deposits charge at $R(E_b)$ when all energy is expended (see Fig. 4). Figure 2(a) shows the results of a composite model for the energy dependence of the range spanning from a few eV to 10^7 eV [9]. It is important to be able to approximate the range in this broad energy regime due to the nature of the space environment where the energies of the space plasma fluxes generally lie between ~10 eV and ~10 MeV [1]. Note that for a dielectric held at potential V, the range is actually a function of the "landing energy" $[E_b+q_eV]$, rather than E_b. (q_e<0 is the charge on an electron.) Also, it is important to note that

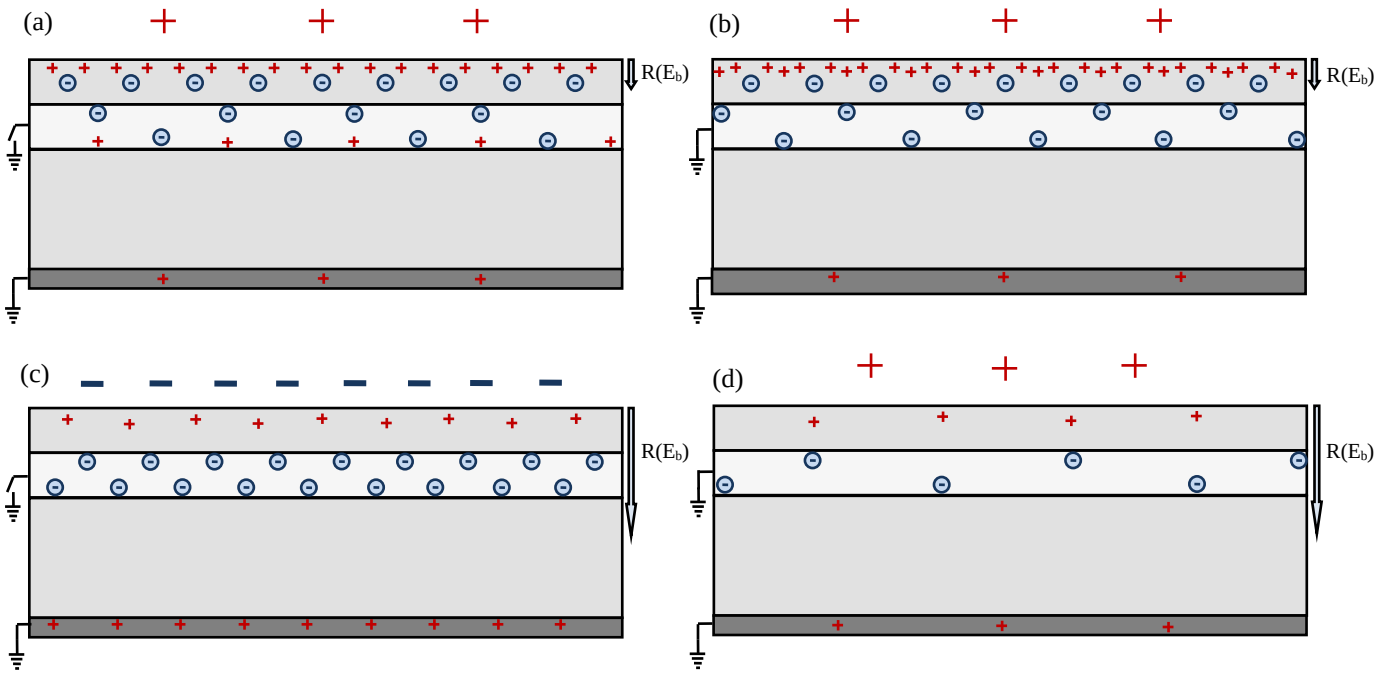

Fig. 6. Charging models for a multilayer dielectric with a conducting middle layer: (a) surface dielectric deposition with low energy electron beam and ungrounded conductive layer, (b) surface dielectric deposition with low energy electron beam and grounded conductive layer (c) conductive layer deposition with high energy electron beam and ungrounded conductive layer (d) conductive layer deposition with high energy electron beam and grounded conductive layer. Electrons are shown as blue circles ⊖ and positive charge centers (holes) are shown as red +. Positive (a, b, d) and negative (c) surface voltages are indicated.

electrons for a monoenergetic beam are not all deposited at a single depth, but rather measurements [2] and modeling [8] show there is a distribution of penetration depths sharply peaked near $R(E_b)$. For the present purposes, the charge layer approximation is sufficient.

Knowing the range of electrons becomes especially critical when dealing with multilayer materials, where the incident energy will determine where and in what layer charge and energy are deposited. The low (200 eV) and high (5 keV) incident energies were selected for these experiments based on range calculations to deposit charge near the surface of the surface dielectric and the conductor and into the conductive layer, respectively.

B. Electron Yield

The total electron yield is defined as the ratio of emitted to incident flux and is highly energy dependent [18]. The incident flux is the total number of electrons entering the material from the environment; the emitted flux is the sum of backscattered and secondary electrons, as shown in Fig. 4. Secondary electrons conventionally have energies <50 eV, while backscattered electrons conventionally have energies >50 eV. Backscattered electrons undergo a quasi-elastic collision near the surface and backscatter, imparting no net charge to the material. Secondary electrons are generated by incident electrons that undergo collisions near the surface, which impart energy to several other electrons in the material. Some of these other electrons then escape the material's surface leading to net charge loss. When the total yield is less than unity, charging is negative. When the total yield exceeds unity, the material's surface becomes positively charged due to a deficit of electrons. As the net surface potential reaches a potential of a few volts positive, some secondary electrons are re-attracted to the surface which then can recombine with electron holes. This re-attraction effectively creates an upper limit on the net surface potential in the positive net surface potential charging regime.

As with the range, the yield is actually a function of the "landing energy" $[E_b+q_eV]$ rather than E_b. Dynamic emission models provide models for yield as a function of surface voltage or charging. A simple model for surface voltage (or time) dependence of the yield for negative charging for $E_b>E_2$, based on a charging capacitor was proposed by Thomson [M]:

$$\text{for } 0 \geq q_e V_s(t) \geq (E_2 - E_b) \qquad (1)$$

τ_Q is a decay constant for the exponential approach of the yield to unity, as charge $Q(t)$ is accumulated with elapsed time and E_2 is the crossover energy.

C. Conductivity

The conductivity of a material determines how easily a deposited charge layer can move through the material in response to an electric field, ; each term can be time-dependant. These electric fields, F, are produced by the embedded charge layers, the depletion layer, and the conductive planes in the material as modeled in Figs. 5 and 6. The measured currents will have two terms, a particle current conductivity proportional to the conductivity and a displacement current due to the change in the electric field due to charge accumulation:

For conditions considered here, we assume the conductivity has only two terms, the equilibrium (dark current) conductivity and radiation induce conductivity; we neglect contributions for polarization, diffusion and dispersion based on arguments related to the time dependence of these

contributions compared with our experimental times [20]. For low electron fluxes the conductivity, , is a static conductivity that approaches the equilibrium (dark current) conductivity of the material, . For fused silica the equilibrium conductivity at room temperature is $\approx 1.5 \cdot 10^{-19}$ $(\Omega\text{-cm})^{-1}$ [23]. Because of fused silica is so low, charge movement over the duration of our tests can be neglected and we can assume perfect insulators as a first order approximation for our models.

For high fluxes, however, Radiation Induced Conductivity (RIC) must be taken into account in regions where the incident beam penetrates. RIC is the enhanced conductivity that results from the energy deposited in this volume. RIC is a function of the dose rate, , which is the power deposited by incident radiation per unit mass [21]:

(2)

The dose rate in a homogeneous material is approximately inversely proportional to the volume in which radiation energy is deposited; this volume is approximately equal to the beam cross sectional area times R [22]: therefore,

(3)

Where J_b is the incident beam current density and ρ_m is the mass density. The dose rates for disordered SiO_2 and Ag as a function of incident energy are shown in Fig. 3(a). RIC is expressed in terms of the dose rate as a power law with $\frac{1}{2} < \Delta < 1$ [21]. Figure 3(b) shows the RIC for SiO_2 as a function of incident energy. Notice that both and σ_{RIC} exhibit energy dependent maxima as a consequence of the minimum in the range expression seen in Fig. 2(a). For fused silica $\Delta \approx 1$ and $\approx 1.7 \cdot 10^{-16}$ $(\Omega\text{-cm-rad/s})^{-1}$ at room temperature [23]. For the low and high energy tests, is approximately $1 \cdot 10^{-10}$ $(\Omega\text{-cm})^{-1}$ at J_b=20 nA/cm^2 and $1 \cdot 10^{-12}$ $(\Omega\text{-cm})^{-1}$ at J_b=2 nA/cm^2, respectively. Because these values are relatively high, the charge bodies will reach equilibrium in the RIC region on smaller time scales than we can detect. To calculate the deposited power for each layer we can multiply Eq. 3 by the amount of material radiated and, for subsequent layers, replace E_b with the energy at which the electrons enter that particular layer. Figure 3(c) shows the deposited power for our multilayered samples as a function of incident energy.

Surface Potential

Using these three physical phenomena we can now build a model to relate the internal charge distribution to the net surface potential. Once an insulator with a grounded backplane is exposed to an electron flux, to first order, the surface potential charges according to a simple capacitance model [3,20]

(4)

where is permittivity of free space, is the relative permittivity of the material, and , the long term equilibrium potential, is

(5)

Where is the incident beam current density corrected for the duty cycle. For the experiments here, thus the exponential term in Eq. (4) can be neglected. To account for the charge dependant electron emission given by Eq. (1), we write the injection voltage as [20]

(6)

An additional effect to account for is the re-attraction of secondary electrons to the charged surface [24]. For negative surface potentials at which Y>1, these emitted electrons will receive a "boost" in energy of $|q_e V_s|$ as they leave the surface; the number of emitted electrons is largely unaffected by negative surface potentials. As the material charges more and more negatively, the deposited charge layer can produce an electric field which exceeds the limits of the material, leading to electrostatic breakdown. This breakdown voltage may or may not be reached, depending on the conductivity of the material and the current density of the electron beam. If the charge dissipation to ground can keep pace with the amount of charge deposited, then the material will reach an equilibrium voltage lower than the breakdown voltage. When breakdown does occur, conduction paths may be formed which then decrease the materials ability to hold charge. This will lead to a negative net surface potential less than the original net surface potential before breakdown. For fused silica at room temperature, the dielectric breakdown strength is $\sim 3.5 \cdot 10^7$ V/m and the relative permittivity for fused silica is 3.5 [23].

For negative surface potentials at which Y<1, however, more electrons are ejected from near the surface than penetrate into the material. A depletion charge layer forms that is more positive than the deeper negative charge layer deposited by the electron beam. As the net surface potential becomes more positive, the emitted secondary electrons become re-attracted to the surface, where they can recombine with depletion sites (holes). By convention secondary electrons have less than 50 eV emission energy; emission spectra for essentially all uncharged materials are peaked at ~2 eV to 5 eV and the vast majority of emitted secondary electrons have energies <10 eV. Since secondary electron emission spectra are peaked at low energies, even small positive surface potentials re-attract large numbers of secondary electrons; this means that positive potentials are self-limiting and seldom exceed ~10 V.

The charging scenarios described above are often described by a double dynamic layer model (DDLM) [25, 26, 27]. The DDLM model has been used to describe static measurement of surface voltage [3] and electron yields [18]. A discussion of the dependence of satellite charging in terms of threshold charging due to re-attraction and changes in the yield is presented in [28].

D. Electrode Current

The current measured at the grounded rear electrode includes two contributions, the free charge transport current density, J_c, and the charge displacement current density, J_{disp}.

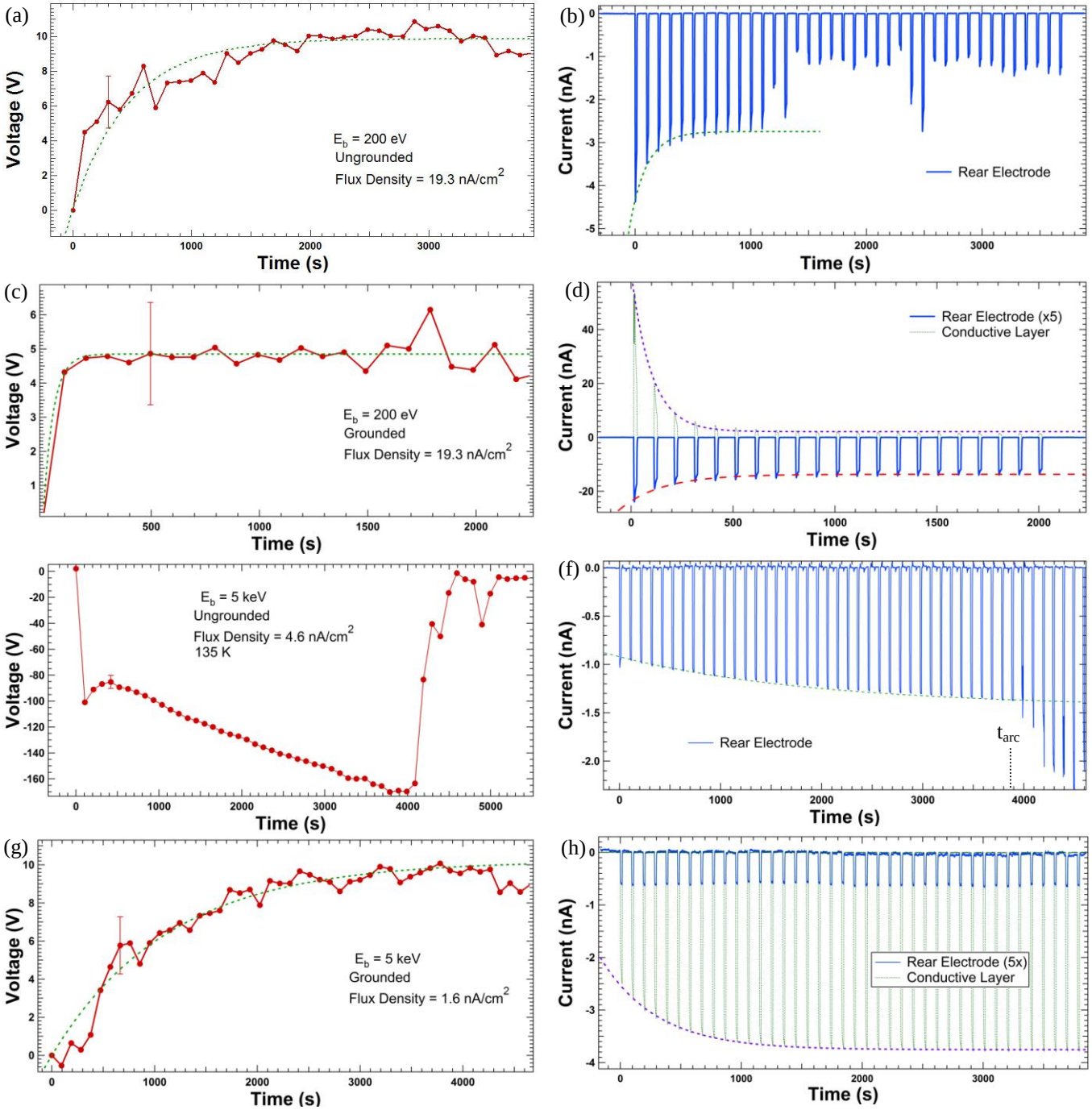

Fig. 7. Measurements of surface potentials vs time (a, c, e, g) and rear electrode and conductive layer currents vs time (b, d, f, h) for: (a, b) surface dielectric deposition with low energy electron beam and ungrounded conductive layer; (c, d) surface dielectric deposition with low energy electron beam and grounded conductive layer; (e, f) conductive layer deposition with high energy electron beam and ungrounded conductive layer; and (g, h) conductive layer deposition with high energy electron beam and grounded conductive layer. (a,b,c,d,g,h) were measured at 298 K and (e,f) at 135 K. Exponential fits for the voltage was based on Eq. 6 with (a) τ=475 s (τ_Q =6.6 μC), (c) τ=45 s (τ_Q =0.63 μC), (g) τ=1137 s (τ_Q =1.33 μC). Exponential fits for the currents were based on Eq. 8 with (b) τ=139 s (τ_Q =1.93 μC), (d) conductive layer τ=99 s (τ_Q =1.37 μC), rear electrode τ=206 s (τ_Q =2.86 μC) (f) τ=2880 s (τ_Q =3.37 μC), (h) τ=462 (τ_Q =0.54 μC).

(7)

For the time independent conductivity estimated above and for general voltage expressions for the parallel plate geometry, it can be shown that this current is given by [20]

(8)

IV. Results

The surface voltage and rear electrode and conducting layer current data presented in Fig. 7 correspond to the four scenarios identified in Section III; (A) surface dielectric deposition (with 200 eV electron beam) with ungrounded conductive layer; (B) surface dielectric deposition (with 200 eV electron beam) with grounded conductive layer; (C) conductive layer deposition (with 5 keV electron beam) with

grounded conductive layer; and (D) conductive layer deposition (with 5 keV electron beam) with ungrounded conductive layer. Results and fits for each of the four scenarios are given in the four sections below, along with discussions of their similarities and differences and interpretation of the results in terms of the model of Section III.

A. Surface Dielectric Deposition—Ungrounded

For a 200 eV monoenergetic electron beam the electron range in disordered SiO_2 is approximately 3 nm, as shown in Fig. 2(a). At this depth, the electrons just penetrate into the first layer, but do not reach the conductive layer. From Fig. 2(b) the total yield for disordered SiO_2 at this energy is ~1.3>1, which leads to a positive charge depletion layer. Thus, we should see a self-limiting positive net surface potential due to a net deficit of electrons; this agrees with the sign of the measured net surface potential as shown in Fig. 7(a). Voltage equilibrium is reached after ~2000 s at V_o=9.9±0.5 V, which is only ~4% of the beam voltage and is consistent with re-attraction of most secondary electrons to the positively charged surface. V_s and J_{elec} (see Eqs. (6) and (8), respectively) are both reduced by ~96% from incident current (J_b) values, which is the product of a duty cycle factor [t_{on} / (t_{on} + t_{off})] = 15% and a yield factor [1-Y(200eV)] ≈ 30%. The magnitude of the equilibrium voltage predicted by this reduction factor is ~80% of the measure V_0. The magnitude of the displacement current predicted by this reduction factor is ~60% of the measured displacement current amplitude of ~1.58 nA in Fig. 7(b).

The surface voltage data in Fig. 7(a) is fit well by an exponential decay from Eq. (6), with decay time constant τ=475±50 s or in terms of *incident charge*, τ_{QI}=6.6 μC. Comparison with the yield data dependant on *deposited charge* in Fig. 2(c) with a charge constant τ_{QD}=56 fC suggests that only 15 ppb of the incident charge is absorbed. Because the conductive layer is ungrounded, a charge separation in the metal will occur due to the electric field produced in by the top layer, but it will have negligible effect on the net surface potential.

Figure 7(b) shows the rear electrode current as a function of time. The "comb" structure of the current data clearly reflects the current duty cycling with t_{on}=15 s and t_{off}=84 s. The mean values of the rear electrode current in each current spike shows a long term saturation as expressed as an exponential decay (solid curve in Fig. 7(b)) as modeled by a simplified version Eq. (8) with J_{sat}= ; the displacement term is neglected due to the long time scales between surface voltage measurements. Fused silica has very low dark current conductivity of ~$3\cdot10^{-19}$ (ohm-cm)$^{-1}$ [23] with a corresponding decay time of ~$1\cdot10^{6}$ s; so charge movement from the layer deposited at $R(E_b)$ to the conducting layer is negligible on the 10^3 s time scale of our measurements, but our fits require an extra additive offset constant, J_{offset}. Thus we must have a significant charge dissipation mechanism active such as polarization, RIC, an arc-induced leakage path, or surface leakage currents. Results show that our saturation current is J_{sat}=1.58 nA, with offset, J_{offset}=-4.34 nA giving current equilibrium J_{eq}= J_{sat}+ J_{offset} =-2.76 nA and decay time constant τ_D=139±12 s or in terms of incident charge, τ_Q=1.9 μC. The significant variations evident in the rear electrode current (Fig. 7(b)) after ~1200 s suggest that sustained small-scale arcing begins in the ungrounded conducting layer.

One thing of interest for this test is the direction of current flow. Generally, we would expect to see a positive current on our electrometer associated with electrons entering the material to counteract the net positive potential produced in the surface dielectric. A possible explanation is due to the middle conductive layer being exposed on the edge of the sample. Because the beam is Gaussian, there exists a plasma of electrons in the gap between the sample holder and this exposed edge creating a leakage path through this diffuse plasma. This allows the conductive layer to charge slightly negative creating an overall negative potential below the conductive layer which then causes electrons to flow from the rear electrode and produce the current seen in Fig 7(b).

Closer examination of the rear electrode current for a single pulse clearly shows this displacement current along with a saturation current. Thus, an exponential fit to the current decay for a single pulse is the summation of the exponential of the short term saturation current plus the exponential of the displacement current as modeled in Fig. 9(a). For surface dielectric deposition, the exponential displacement has a time constant of 4.1±0.1 s (0.38 ± 0.09 μC) while the saturation time constant is 1 ± 1 (0.1 ± 0.1 μC) which is much longer than the time constant for RIC conduction, τ_{RIC}=6 ms based on Eq. (2), the beam parameters, and a literature value of RIC [23]. Thus, we speculate that charge motion during the beam on times is driven, at least in large part something besides RIC conduction or that the literature value is inaccurate for the specific type of disordered SiO_2 used in our experiments.

B. Surface Dielectric Deposition—Grounded

For a 200 eV electron beam with a grounded conductive layer, we expect similar behavior for the surface voltage as seen for the ungrounded scenario.

Positive surface voltage is observed in Fig. 7(c), as expected. Voltage equilibrium is reached after ~400 s at V_o=4.8±0.4 V, fit well by an exponential decay from Eq. (6), with decay time constant τ=45±14 s (0.6 ± 0.2 μC). It is speculated that the decay time constant is an order of magnitude smaller than the ungrounded case due to the image charge plane formed in the grounded conducting layer.

Because electrons are free to move from ground to the conductive plane, we should see a positive current on the electrometer into the conductive layer to form this image plane. This is seen in the conductive layer current in Fig. 7(d). Note that the initial current for the uncharged sample is ~52 nA, is also approximately half of the estimated incident current for an incident current density of ~19 nA/cm^2 and a sample collection area of 4.9 cm^2. The current falls off exponentially with a long-term saturation time constant of 99±4 s (1.37 ± 0.05 μC) while the rear electrode current for the grounded case has long term saturation time constant τ=206±30 s (2.9 ± 0.4 μC). These fitting parameters are within ~30% of those found for the ungrounded case. This long term saturation current is driven by the equal magnitude mirror charge layer on the metal layer at a distance only ~240 nm (~100 ppm) closer to the rear electrode than for the ungrounded case.

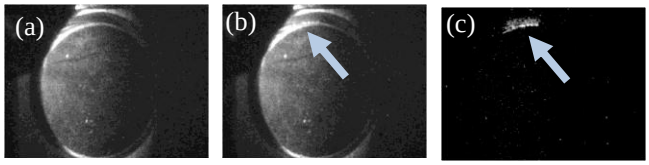

Fig. 8. Visible images of sample with the CCD video camera (a) immediately before the arc (b) during the arc. (c) the first image subtracted from arc image to show the light attributed to the arc. Arrow indicates location of visible arc

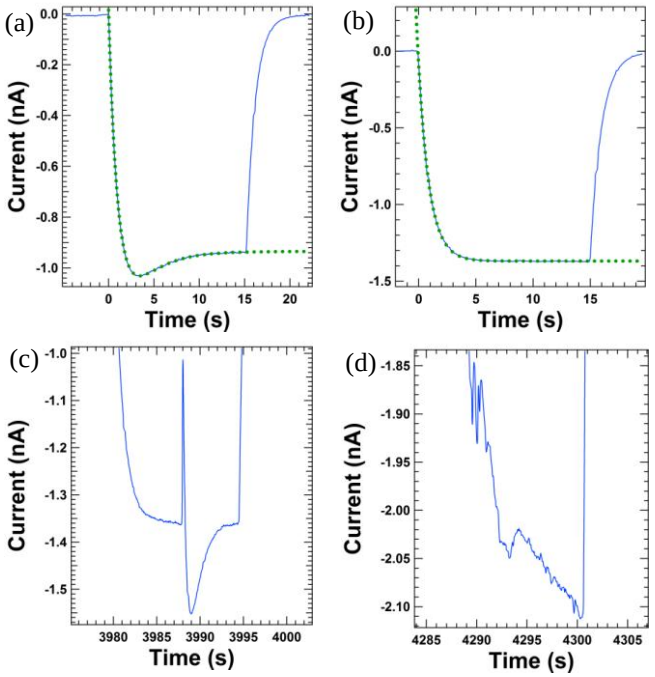

Fig.9. Expanded views of the rear electrode current in Fig. 7(f) for conductive layer deposition with high energy (5 keV) electron beam and an ungrounded conductive layer that is undergoing negative charging. A similar profile is seen in both low energy (200 eV) surface substrate deposition cases in Figs. 7(b) and 7(d). (a) First current pulse with fit based on Eq. 8. (b) Current pulse immediately before the first observed arc with fit based on Eq. 8. (c) Current during first arc. (d) Current after subsequent arcing.

C. *Conductive Layer Deposition—Grounded*

For a 5000 eV monoenergetic electron beam the electron range in disordered SiO_2 is ~560 nm, as shown in Fig. 2(a). At this depth, the electrons penetrate through the surface dielectric and into the conductive layer. The incident current was reduced to ~1.6 nA/cm^2 for the high energy beam. The total yield for disordered SiO_2 (see Fig. 2(b)) at this energy is ~0.7<1, which should lead to a negative net surface potential in Fig. 7(g). However, because the conductive layer is grounded, charge will dissipate quickly from the conductive layer. Although the electron yield is <1 for a 5 keV electron beam, there will still be a positively charged deficit layer near the surface which will behave similar to the low energy scenarios, thus we should observe a self-limiting small positive potential similar to Fig. 7(a). This is confirmed in Fig. 7(g), where voltage equilibrium is reached after ~2000 s at V_o=9.3±0.4 V. The surface voltage data in Fig. 7(g) is fit well by an exponential decay from Eq. (6), with decay time constant τ=1137±93 s (1.3 ± 0.1 μC), which agrees with the fitting parameters in Fig. 7(a) to within 80±%.

Figure 7(h) shows constant, negative and nearly zero rear electrode current; this is expected since the conductive layer is held at ground and excess charge is bled off. This current on the conductive layer can be modeled as an exponential decay (solid curve in Fig. 7(h)), based on Eq. (8), with saturation current J_{sat}=1.22 nA, equilibrium current J_{eq}=*-3.76* and decay time constant τ=462 ± 11 s (0.54 ± 0.01 μC).

D. *Conductive Layer Deposition—Ungrounded*

For a 5 keV electron beam with an ungrounded conductive layer, we expect significantly different behavior than seen for the surface voltage with a grounded conductive layer. The high energy incident electrons deposit negative charge in the conductive layer. Because the conductive layer is ungrounded there will be no fast charge dissipation mechanism. Because there is no limiting behavior from re-attraction of secondary electrons, we should see a high net negative potential. Because of the low conductivity, the charge cannot dissipate through the dielectric substrate to the grounded rear electrode faster than charge is being deposited by the beam, thus the potential will become more and more negative until the produced electric fields exceed the limits of the material or produce fields strong enough to produce arcing from the exposed surface of the conductive layer to the surrounding grounded sample holder ~2 mm away.

The surface voltage will increase linearly with time (or more correctly incident charge), at least until the sample acquires potential approaching the incident beam voltage where charge deposition begins to be suppressed. This behavior is shown in Fig 7(e) where the material continued to charge negative in a linear fashion until electrostatic discharge from the conductive layer to the sample holder was observed in both the imaging instruments (see Fig. 8) and the electrometer (see Fig. 9). For the first charge pulse the sample reaches ~-100 V; this is a charging rate of ~10% of that if all incident charge were deposited; this factor of 0.1 may result from either the leakage currents noted above or from a reduction of the incident current by a factor of $[1-Y(E_b+q_eV)]$which is ~0.3 for 4830 V. At this charging rate the surface voltage would reach ~-170 V during the second pulse. While not obvious from the rear electrode current or visual data, we speculate that a breakdown or discharge pulse occurs during the second pulse; this is similar to other ungrounded 5 keV runs where an obvious discharge occurred during the first or second pulses which led to a subsequent decrease in the surface voltage. After the third or fourth pulse, the surface voltage again shows a linear increase, but now at a charging rate ~40 times less than the initial rate. The reduction in rate is hypothesized to have resulted from enhanced conduction paths caused by the arcing. The linear charging at the lower rate continues until ~4000 s at which point the sample again reaches ~-170 V and another discharge occurs; this time the arc is obvious in the rear electrode current as seen in Fig. 9 (c). At this point there is a significant change observed in both the surface voltage and rear electrode current. The surface voltage decreases significantly and becomes more erratic; after ~5000 s only very small negative voltages can be sustained. The rear electrode current is initially constant and equal to ~100% of the incident current. After the large arcing event at ~4000 s, the current begins to increase somewhat and becomes much more erratic, suggesting electrostatic breakdown of the material, as seen in the electrometer data in Fig. 9 (d). Inspecting the separate pulses we see that there is an obvious displacement current for the first beam pulse as shown in Fig.

9(a), with exponential displacement time constant 0.507 ± 0.008 s (4.0 ± 0.06 nC) and saturation exponential time constant 1.444 ± 0.007 s (11.3 ± 0.06 μC). After a few beam pulses the displacement current vanishes as shown in Fig. 9(b), with saturation exponential time constant 0.966 ± 0.001 s (7.53 ± 0.007 nC) which is a change of ~30%.

V. Conclusion

Through observation of the net surface potential and the currents from the rear electrode and the conducting plane (when grounded), we have been able create a model to infer the internal charge distribution. The results showed that the four scenarios of ungrounded dielectric surface deposition, grounded dielectric surface deposition, ungrounded conductive layer deposition and grounded conductive layer deposition led to two net surface potential charging regimes, namely small positive charging and high negative charging. From this we can predict the resulting electric fields in the material to help determine the potential of electrostatic breakdown which was observed in several runs. While the net surface potential showed the charge equilibrium reached after a given pulse, the electrometer data showed the time evolution of the charges as they reached the aforementioned equilibrium. This gave information about displacement currents, charging internal floating conductors and signs of arcing.

Clearly the combination of surface voltage and electrode current measurements coupled with an accurate model of the evolving charge distribution provide valuable tools to understand both laboratory tests and actual spacecraft charging and arcing events.

ACKNOWLEDGEMENT

We gratefully acknowledge contributions to instrumentation and experimental efforts from Josh Hodges, Robert Johnson, Tamara Jeppsen and Doug Ball of the Materials Physics Group, Michael Taylor for the use of infrared and CCD video cameras, aid with theoretical models from Alec Sim, and useful discussions with Robert Meloy and Charles Bowers of NASA Goddard Space Flight Center.

References

[1] D. Hastings, H. Garrett, Spacecraft-Environment Interactions, New York, NY: Cambridge Press, 1996.

[2] B. Beecken, B. Walling, "Modeling of Deep-dielectric Spacecraft Charging in Realistic Environments with NUMIT2" AIAA 2011 3975

[3] J.L. Hodges, "*In Situ* Measurements of Electron Beam Induced Surface Voltage of Highly Resistive Materials," MS Thesis, Dept. Physics, Utah State University, Logan, UT, 2012.

[4] Joshua L. Hodges, Alec M. Sim, Justin Dekany, Gregory Wilson, Amberly Evans, and JR Dennison "*In Situ* Surface Voltage Measurements of Layered Dielectrics," *Proc. of the* 12*th Spacecraft Charging Techn. Conf.,* (Kitakyushu, Japan, May 14-18, 2012).

[5] A.R. Frederickson and J.R. Dennison, "Measurement of Conductivity and Charge Storage in Insulators Related to Spacecraft Charging," *IEEE Transaction on Nuclear Science*, Vol. 50, No. 6, December 2003, pp. 2284-2291.

[6] L. Levy, D. Sarrail, and J. M. Siguier, "Conductivity and secondary electron emission properties of dielectrics as required by NASCAP," *Third European Symposium on Spacecraft Materials in Space Environment*, 1993, pp. 113-123.

[7] R. Coelho, L. Levy, and D. Sarrail, "Charge decay measurements and injection in insulators," *Journal of Applied Physics*, Vol. 22, No. 9, Sept. 1989, pp. 1406-1409.

[8] Wousik Kim, "NUMIT 2.0: The official release of the JPL's internal charging code," *Proc. of the* 12*th Spacecraft Charging Techn. Conf.,* (Kitakyushu, Japan, May 14-18, 2012).

[9] G. Wilson and JR Dennison, "Approximation of Range in Materials as a Function of Incident Electron Energy," IEEE Transaction on Plasma Science, *IEEE Trans. on Plasma Sci.*, **40**(2), 305-310 (2012).

[10] RC Hoffmann and JR Dennison, "Methods to Determine Total Electron-Induced Electron Yields Over Broad Range of Conductive and Nonconductive Materials," *IEEE Trans. on Plasma Sci.*, **40**(2), 298-304 (2012).

[11] Justin Dekany, Alec M. Sim, Jerilyn Brunson, and JR Dennison, "Electron Transport Models and Precision Measurements in a Constant Voltage Chamber," *Proc. of the* 12*th Spacecraft Charging Techn. Conf.,* (Kitakyushu, Japan, May 14-18, 2012).

[12] Charles Sim, Alec M. Sim, JR Dennison and Matthew Stromo, "Defect-Driven Dynamic Model of Electrostatic Discharge and Endurance Time Measurements of Polymeric Spacecraft Materials," *Proc. of the* 12*th Spacecraft Charging Techno. Conf.,* (Kitakyushu, Japan, May 14-18, 2012).

[13] JR Dennison, "The Dynamic Interplay Between Spacecraft Charging, Space Environment Interactions and Evolving Materials," *Proc. of the* 12*th Spacecraft Charging Techn. Conf.,* (Kitakyushu, Japan, May 14-18, 2012).

[14] W.Y. Chang, J.R. Dennison, Neal Nickles and R.E. Davies, "Utah State University Ground-based Test Facility for Study of Electronic Properties of Spacecraft Materials," *Proc. of the 6th Spacecraft Charging Techn. Conf.*, (Air Force Research Laboratory Science Center, Hanscom Air Force Base, MA, 2000).

[15] Amberly Evans, Gregory Wilson, Justin Dekany, Alec M. Sim and JR Dennison "Low Temperature Cathodoluminescence of Space Observatory Materials," *Proc. of the* 12*th Spacecraft Charging Techn. Conf.,* (Kitakyushu, Japan, May 14-18, 2012).

[16] J.Dekany, R. H. Johnson, G. Wilson, A. Evans and JR Dennison, "Ultrahigh Vacuum Cryostat System for Extended Low Temperature Space Environment Testing," *Proc. of the* 12*th Spacecraft Charging Techn. Conf.,* (Kitakyushu, Japan, May 14-18, 2012).

[17] C.D. Thomson, V. Zavyalov, and J.R. Dennison, "Instrumentation for Studies of Electron Emission and Charging from Insulators," *Proceedings of the 8th Spacecraft Charging Techn. Conf.* (NASA Marshall Space Flight Center, Huntsville, Al, October 2003), 15 pp.

[18] R. Hoffmann, "Electron-Induced Electron Yields of Uncharged Insulating Materials, " M.S. Thesis, Dept. Physics, Utah State University, Logan, UT, 2010.

[19] C. Thomson, "Measurements of the Secondary Electron Emission Properties of Insulators," Ph.D. Dissertation, Dept. Physics, Utah State University, Logan, UT, 2004.

[20] JR Dennison and Alec M. Sim, "Unified Density of States Based Model of Electron Transport and Emission of Spacecraft Materials," *Proc. of the* 12*th Spacecraft Charging Techn. Conf.,* (Kitakyushu, Japan, May 14-18, 2012).

[21] J.R. Dennison, J. Gillespie, J.L. Hodges, R.C. Hoffmann, .J. Abbott, A.W. Hunt and R. Spalding, "Radiation Induced Conductivity of Highly-Insulating Spacecraft Materials," in *Application of Accelerators in Research and Industry*, Am. Instit. Phys. Conf. Proc. Series, Vol. 1099, ed. F.D. McDaniel and B. L. Doyle, (Am. Instit. of Phys., Melveille, NY, 2009), pp. 203-208.

[22] J.A. Roth, R. Hoffmann, and J.R. Dennison, 2009, "Effects of Radiation Induced Conductivity on Electrostatic Discharge in Insulating Materials," in Proc. 1st AIAA Atmospheric and Space Environments Conf. (San Antonio, TX).

[23] V.E Culler and H.E. Rexford, "Gamma-radiation-induced conductivity in glasses," Proc. IEE, 112(7), 1462, 1965

[24] N. Nickles, R.E. Davies and J.R. Dennison, "Applications of Secondary Electron Energy- and Angular-Distributions to Spacecraft Charging," *Proc. of the 6th Spacecraft Charging Techn. Conf.,* (Air Force Research Laboratory Science Center, Hanscom Air Force Base, MA, 2000).

[25] J. Cazaux, "Scenario for Time Evolution of Insulator Charging under Various Focused Electron Irradiations," *J. Appl. Phys.* **95**, 731, 2003.

[26] A. Melchinger and S. Hofmann, "Dynamic Double Layer Model: Description of Time Dependent Charging Phenomena in Insulators under Electron Beam Irradiation," *J. Appl. Phys.* **78**, 6224, 1995.
[27] X.D. Meyza, Goeuriot, C. Guerret-Piecourt, D. Treheux, and H. Fitting, "Secondary Electron Emission and Self-Consistent Charge Transport and Storage in Bulk Insulators: Application to Alumina," *J. Appl. Phys.* **94**, 5384, 2003.
[28] JR Dennison, R.C. Hoffmann, and J. Abbott, "Triggering Threshold Spacecraft Charging with Changes in Electron Emission from Materials," Paper AIAA-2007-1098, *Proc. of the 45th Am. Inst. of Aeronautics and Astronomics Meeting on Aerospace Sci.*, Reno, NV, January, 10, 2007.

Greg Wilson is currently a graduate student at Utah State University in Logan, UT pursing an MS in physics. He received BS degrees in physics and mathematics from USU in 2011. He has worked with the Materials Physics Group for two years on electron emission and luminescence studies related to spacecraft charging. He also developed a composite model for electron range over a wide range of incident energies applicable to diverse materials.

JR Dennison received the B.S. degree in physics from Appalachian State University, Boone, NC, in 1980, and the M.S. and Ph.D. degrees in physics from Virginia Polytechnic Institute and State University (Virginia Tech), Blacksburg, VA in 1983 and 1985, respectively. He was a Research Associate with the University of Missouri—Columbia before moving to Utah State University (USU), Logan, UT in 1988. He is currently a Professor of physics at USU, where he leads the Materials Physics Group. He has worked in the area of electron scattering for his entire career and has focused on the electron emission and resistivity of materials related to spacecraft charging for the last two decades.

Amberly Evans is currently a graduate student at Utah State University in Logan, UT pursing an MS in physics. She received BS degrees in physics and chemistry from USU in 2012. She has worked with the Materials Physics Group for five years on electron emission, luminescence and resistivity studies and on MISSE retrieval and post-flight analysis of *SUSpECS*. Much of her work has focused on optical scattering of spacecraft materials.

Justin Dekany is currently a graduate student at Utah State University in Logan, UT pursing an MS in physics. He received a BS degree in physics from USU in 2010. He has worked with the Materials Physics Group for four years on electron transport measurements, electrostatic discharge tests, electron emission measurements, and luminescence studies related to spacecraft charging. He has been the Lab Manager for the Materials Physics Group for the last two years.